The Astrophysical Journal, 926:118 (12pp), 2022 February 20 https://doi.org/10.3847/1538-4357/ac43bf

Searching for New Observational Signatures of the Dynamical Evolution of Star Clusters

B. Bhat[1,2], B. Lanzoni[1,2], F. R. Ferraro[1,2], and E. Vesperini[3]
[1] Dept. of Physics and Astronomy "A. Righi", University of Bologna, Via Gobetti 93/2, Bologna, Italy
[2] INAF Osservatorio di Astrofisica e Scienza dello Spazio di Bologna, Via Gobetti 93/3, Bologna, Italy
[3] Dept. of Astronomy, Indiana University, Bloomington, IN 47401, USA
Received 2021 October 8; revised 2021 December 14; accepted 2021 December 14; published 2022 February 17

Abstract

We present a numerical study, based on Monte Carlo simulations, aimed at defining new empirical parameters measurable from observations and able to trace the different phases of the dynamical evolution of star clusters. As expected, a central density cusp, deviating from the King model profile, develops during the core collapse (CC) event. Although the slope varies during the post-CC oscillations, the cusp remains a stable feature characterizing the central portion of the density profile in all post-CC stages. We then investigate the normalized cumulative radial distribution (nCRD) drawn by all the cluster stars included within one half of the tridimensional half-mass radius ($R \leqslant 0.5r_h$), finding that its morphology varies in time according to the cluster's dynamical stage. To quantify these changes we defined three parameters: A_5, the area subtended by the nCRD within 5% of the half-mass radius, P_5, the value of the nCRD measured at the same distance, and $S_{2.5}$, the slope of the straight line tangent to the nCRD measured at $R = 2.5\%r_h$. The three parameters evolve similarly during the cluster's dynamical evolution: after an early phase in which they are essentially constant, their values rapidly increase, reaching their maximum at the CC epoch and slightly decreasing in the post-CC phase, when their average value remains significantly larger than the initial one, in spite of some fluctuations. The results presented in this paper suggest that these three observable parameters are very promising empirical tools to identify the star cluster's dynamical stage from observational data.

Unified Astronomy Thesaurus concepts: Star clusters (1567); Globular star clusters (656); Dynamical evolution (421); Computational methods (1965); Stellar dynamics (1596)

1. Introduction

Globular clusters (GCs) are collisional stellar systems, where frequent gravitational interactions among stars significantly alter the overall energy budget, leading to a progressive internal change in the cluster structure and in the radial distribution and content of objects with different masses: the most massive stars tend to transfer kinetic energy to lower-mass objects (energy equipartition) and progressively sink toward the system center (dynamical friction and mass segregation); the energy transfer between stars causes the gradual loss (evaporation) of stars (preferentially low-mass ones). The continuous kinetic energy transfer from the core to the outskirts leads to a runaway contraction of the core itself, with a substantial increase in its density toward an infinite value: the so-called "core collapse" (hereafter, CC; see, e.g., Spitzer 1987; Meylan & Heggie 1997). The contraction is thought to be halted by the formation and hardening of binary systems, and the post-CC phase is characterized by several episodes of increasing central density, followed by stages during which the cluster rebounds toward a structure with lower density and a more extended core (the so-called "gravothermal oscillations"; e.g., Meylan & Heggie 1997). Clearly, these processes significantly affect the structure of the system with respect to the initial conditions. Overall, the long-term internal dynamical evolution tends to generate compact clusters, making large-core systems naturally evolve toward objects with progressively smaller core radius (R_c). Concurrently, the radial distribution of stars with different masses progressively varies in time (the most massive objects migrating to the center), and the high-density cluster environment may facilitate the formation of exotic species that are not predicted by stellar evolution theory (such as blue straggler stars, millisecond pulsars, low-mass X-ray binaries, intermediate-mass black holes; e.g., Ferraro et al. 1997; Pooley et al. 2003; Ransom et al. 2005).

The characteristic timescales of these changes depend in a very complex way on the various internal and external properties, such as total cluster mass, initial size, central density, binary fraction, orbit within the Galactic potential well, and so on. Hence, they can significantly differ even in clusters of the same chronological (stellar) age and, within the same system, from high- to low-density regions. Because of such complexity, the observational identification of the evolutionary stage reached by a cluster (i.e., its "dynamical age") may be hard and lead to ambiguous conclusions. Of course, this may significantly hamper efforts aimed at linking the theoretical predictions concerning the dynamics of star clusters with observations. In this respect, due to their proximity to the Sun, Galactic GCs (GGCs), represent the ideal laboratory (possibly the only place in the universe) where dynamical evolutionary processes can be investigated in thorough detail. The vast majority of these stellar systems are very old ($t = 12$ Gyr, comparable to the age of the universe; see, e.g., Marín-Franch et al. 2009; Forbes & Bridges 2010), but because of different internal and external properties, they sample essentially all the dynamical evolutionary stages expected for multibody and multimass systems.

Until recently, the characterization of the dynamical age of GGCs was essentially based on their structural morphology. In fact, one of the most used indicators, the central relaxation time (t_{rc}), is estimated from the measurement of structural parameters such as the core radius and the central density,

following the analytical expression proposed, e.g., in Equation (10) of Djorgovski (1993, see also Spitzer 1987). These parameters are usually "read" from the King model (King 1966) that best reproduces the projected density profile of a star cluster. Also the classification of GGCs as CC or post-CC systems has so far been based on the detection of a morphological feature, i.e., a steep power-law cusp in the central portion of the density profile (see Djorgovski & King 1984; Ferraro et al. 2003, 2009), strongly deviating from the flat-core behavior of the King model, which well reproduces the density distribution of non-CC clusters. This diagnostic, however, may be not fully reliable since the cusp may be significantly reduced during the post-CC gravothermal oscillations, or due to the occurrence of other processes (e.g., depending on the binary fraction) that may contribute to significantly delaying/reducing the "intensity" of CC, or it can be hardly detectable from observations. As a matter of fact, only a small fraction (15%–20%) of the entire population of GGCs displays a central cusp in the star density profile and is classified as post-CC (see Djorgovski & King 1984; Lugger et al. 1995), in spite of the fact that the central relaxation time is notably shorter than the age in most of the cases (see the compilations by Djorgovski 1993 and Harris 1996).

GGCs also provide the advantage that stars can be resolved and studied individually, thus offering additional possibilities to investigate the internal dynamical state of the system. In principle, either specific classes of objects or the entire cluster population can be used as probes of the cluster dynamical evolution. Indeed, a lot of work in this direction has been done over the last decades. Several theoretical works, mainly based on the results of extensive *N*-body simulations, recently suggested that radial variations of the stellar mass function, the presence of orbital anisotropy, and the velocity dispersion profile as a function of stellar mass can be used to infer the level of energy equipartition and the dynamical state of GCs (e.g., Baumgardt & Makino 2003; Tiongco et al. 2016; Bianchini et al. 2016, 2018; Webb & Vesperini 2017). In turn, these diagnostics are becoming measurable in an increasing number of GGCs, especially thanks to multiepoch Hubble Space Telescope (HST) observations and improved procedures of data analysis, which allow high-precision photometry and measurements of proper motion for stars down to a few magnitudes below the main-sequence turn-off (MSTO). Recent examples of this kind of study can be found, e.g., in Libralato et al. (2018, 2019) and Cohen et al. (2021). While these approaches require observations that, even in the Gaia era, are still very challenging for most GGCs (due to their high central densities and relatively large distances from Earth), our group focused attention on a special class of exotic objects, the so-called blue straggler stars (BSSs), which possibly offer the most promising and viable way to trace the dynamical evolution of dense stellar systems. Being generated by direct collisions (Hills & Day 1976; Lombardi et al. 1995; Sills et al. 2005) or mass-transfer activity in binaries (McCrea 1964; Leonard 1996), they turn out to be significantly heavier ($M_{\rm BSS} = 1.2\ M_{\odot}$; Ferraro et al. 2006; Lanzoni et al. 2007b; Fiorentino et al. 2014; Raso et al. 2019) than the average cluster population ($\langle m \rangle = 0.3\ M_{\odot}$). Hence, these stars are powerful gravitational probes of key physical processes (such as mass segregation and dynamical friction) characterizing the dynamical evolution of star clusters. In fact, the radial distribution of BSSs has been used as a "dynamical clock" to efficiently measure the dynamical aging of stellar systems (Ferraro et al. 2012, 2020; Lanzoni et al. 2016): the level of BSS central segregation with respect to normal (lighter) stars allowed the ranking of GGCs in terms of their dynamical age, from dynamically young systems (with negligible BSS segregation) to highly dynamically evolved clusters, where BSSs are much more centrally concentrated than the reference population (Ferraro et al. 2012, 2018; Lanzoni et al. 2016). The level of BSS central segregation is measured via the A^+ parameter, defined as the area between the cumulative radial distribution of BSSs and that of a lighter, reference population (Alessandrini et al. 2016). A strong correlation between A^+ and the number of relaxation times that have elapsed since cluster formation has been found from the analysis of $\sim 1/3$ of the entire GGC population (Ferraro et al. 2018) and it is confirmed also for a sample of old GCs in the Large Magellanic Cloud (Ferraro et al. 2019).

BSSs have been found to also trace the occurrence of CC and probe the time when it happened. In fact, the double BSS sequence detected for the first time in the post-CC cluster M30 (Ferraro et al. 2009) has been interpreted as the manifestation of the two formation processes, with the bluest sequence being populated by collisional BSSs generated by an enhanced activity of gravitational interactions during CC. Moreover, the measure of the extent of the blue sequence provided the first empirical dating of the CC event (see Ferraro et al. 2009; Portegies Zwart 2019). Since then, the double BSS sequence has been discovered in several additional post-CC clusters (see the cases of NGC 362 in Dalessandro et al. 2013, M15 in Beccari et al. 2019, and NGC 6256 in M. Cadelano et al. 2021, in preparation), thus strengthening the link between this feature and the CC event.

An obvious limitation of using BSSs to infer the dynamical state of the host stellar system is that they are few in number (of the order of a few dozen, on average). Moreover, having different diagnostics of internal dynamical evolution is certainly desirable and useful. Hence, here we analyze the time evolution of a "synthetic GC" obtained from a Monte Carlo simulation run, with the specific aim of defining suitable diagnostics of dynamical aging from a new perspective, i.e., by using the entire population of evolved stars. We provide the definition of three new parameters and test their effectiveness in distinguishing clusters in the pre-CC phase from those experiencing post-CC evolutionary stages, thus tracing the dynamical aging of the system up to CC and beyond. The paper is organized as follows. In Section 2 we describe the initial conditions of the Monte Carlo simulation run and the (observational) approach adopted in the following analysis. Section 3.1 discusses the method used to determine the projected density profile and the best-fit King (1966) model of each extracted snapshot. In Section 3.2 we present the assumptions adopted to build the normalized cumulative radial distributions of cluster stars and discuss the dependence of their morphology on the evolutionary time of the simulation. This is then used in Section 3.3 to define three new empirical parameters able to trace the internal dynamical evolution of stellar systems. Their dependence on the adopted assumptions is discussed in Section 3.4. The summary and conclusions of the work are presented in Section 4.

2. Initial Conditions and Methods

In this work we focus our attention on the dynamical evolution of a star cluster followed with a Monte Carlo simulation run with the MOCCA code (Hypki & Giersz 2013; Giersz et al. 2013). The code includes the effects of binary and stellar evolution (modeled with the SSE and BSE codes; Hurley et al. 2000, 2002) with supernovae kicks assumed to follow a Maxwellian distribution with dispersion equal to 265 km s^{-1} (Hobbs et al. 2005), the effects of two-body relaxation, and a tidal truncation. The initial conditions of the simulation have been chosen well within the range of values observed for GGCs, with the main aim of providing us with a system that experiences all dynamical evolutionary phases and reaches CC within 12–13 Gyr from formation. Since the prime goal of the paper is to put forward the definition of new dynamical indicators, in the following we will present the detailed analysis of this specific run. However, two additional simulations, run from slightly different initial conditions, are discussed in the Appendix, and a much more extensive exploration of the parameter space and its effects on the final results will be the subject of forthcoming dedicated studies (see Section 4 for more details). The simulated cluster has initially 500,000 single stars with masses ranging between 0.1 and 100 $M_\odot$ following a Kroupa (2001) mass function. The initial total mass of the system is $\sim 3.2 \times 10^5$ $M_\odot$, while it is approximately half this value after 12 Gyr of evolution. The stars are initially distributed as a King (1966) model with dimensionless central potential $W_0 = 6$, and the cluster is tidally underfilling, with a tridimensional half-mass radius $r_h = 2$ pc and a Jacobi radius set equal to 61 pc (corresponding to the value the cluster would initially have if orbiting at a Galactocentric distance equal to 4 kpc). No primordial binaries are included in this run, although binary stars dynamically form as the system approaches the CC phase. Since the code includes prescriptions for stellar evolution, it provides for every star at any evolutionary time not only the mass and the three components of position and velocity, but also the magnitude in two photometric bands (namely the V and B bands), from which a color–magnitude diagram of the stellar content at any epoch can be built.

The simulation follows the cluster evolution for $\sim$16 Gyr from its formation. Although this is longer than the Hubble time, it allows us to follow the cluster dynamical evolution also after CC, which occurs at 12.8 Gyr (see below). In Figure 1 we show the time evolution of the cluster's 1% Lagrangian radius ($r_{1\%}$, i.e., the radius including 1% of the total mass of the cluster): the temporal variation of this radius illustrates well the various phases of the cluster's dynamical evolution, and particularly the CC and post-CC phases. The effects of mass loss due to stellar evolution cause the cluster to initially expand as shown by the early increase in $r_{1\%}$. Then, after $\sim$2 Gyr from formation, two-body relaxation starts to drive the evolution of the cluster central region, leading it to a progressive contraction, with $r_{1\%}$ shrinking by approximately a factor of 7 in 10 Gyr. The figure shows that the contraction phase is characterized by an initial "slow phase" ($r_{1\%}$ shrinks by a factor of 2 in approximately 8 Gyr) and a final "rapid phase" (shrinking by a factor of 4, from 0.25 to 0.07 pc, in less than 3 Gyr). At this time, $r_{1\%}$ reaches its minimum value: this is the CC event, occurring at a time $t_{CC} = 12.8$ Gyr. Later, a phase characterized by gravothermal oscillations is clearly distinguishable in the figure, as cyclic expansions and contractions of the 1% Lagrangian radius. Of course, during this evolution, not only the central region, but the entire cluster structure varies with time. To carefully investigate these changes, we extracted 38 time snapshots sampling different evolutionary phases of the system, as marked by the vertical dotted lines in Figure 1. In order to easily and immediately link each snapshot to the corresponding evolutionary phase, we adopted the following color code: *green* for snapshots belonging to the early slow contraction phase, *cyan* for snapshots belonging to the final rapid contraction phase, *blue* for snapshots sampling the CC phase, and *yellow* for snapshots probing the post-CC epoch of gravothermal oscillations.

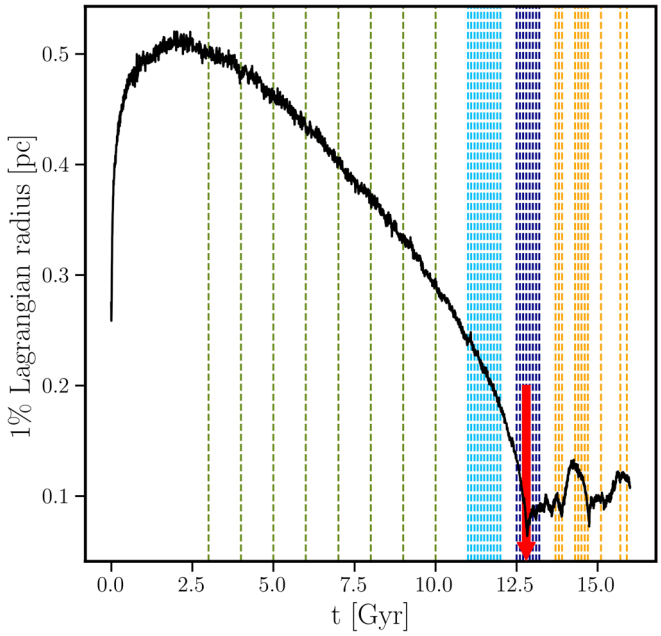

Figure 1. Time evolution of the 1% Lagrangian radius (in parsecs) of the simulated cluster (black line). The vertical lines correspond to the 38 time snapshots analyzed in this work, color-coded as follows to mark different evolutionary stages: green, cyan, blue, and yellow for early, pre-CC, CC, and post-CC, respectively. The time of CC ($t_{CC} = 12.8$ Gyr) is marked with a large red arrow.

In the following analysis, each time snapshot has been studied from an "observational perspective", i.e., as if the simulation output were the product of real observations. This is meant to allow the definition of parameters that can be realistically derived and measured in observational investigations. Thus, procedures and standard strategies, as well as approximations routinely adopted in dealing with observational data, were applied to the snapshots. To this purpose, each snapshot has been projected onto a 2D plane and the distances of all the stars from the cluster's center have been transformed from parsecs to arcseconds assuming that the system is at 10 kpc from the Sun, which is the typical distance of GGCs (Harris 1996; Baumgardt & Vasiliev 2021). We also limited most of the analysis only to stars that are brighter than 0.5–1 magnitudes below the MSTO, in agreement with the threshold adopted in many observational studies to avoid photometric incompleteness biases and to deal with samples of equal-mass stars (see, e.g., Lanzoni et al. 2007a, 2010, 2019; Miocchi et al. 2013).

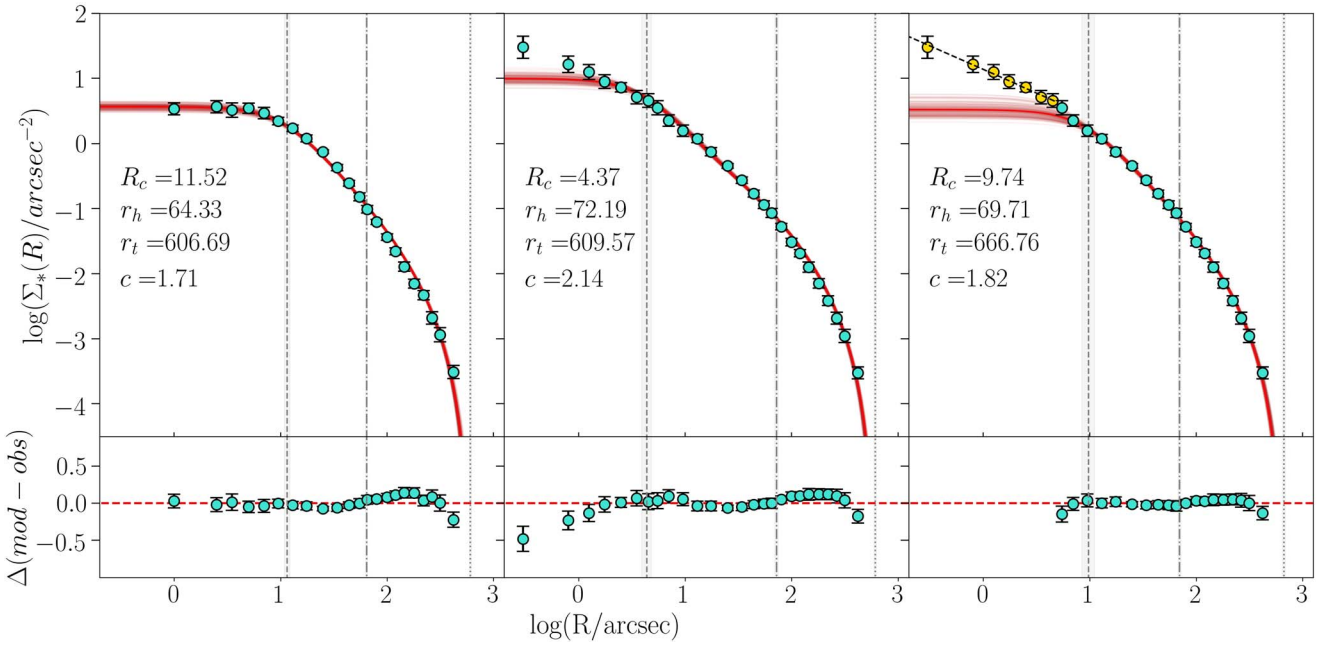

Figure 2. Projected density profile (colored circles), obtained as the number of stars per unit area in different concentric annuli around the cluster center, for two simulation snapshots: a pre-CC cluster at $t = 7$ Gyr (left panel) and a post-CC system at $t = 13.8$ Gyr (central and right panels). The thick red line corresponds to the best-fit King model, while the shaded area marks its uncertainty (see Section 3.1 for the details). The bottom panels show the residuals between the observations and the best-fit King model. For the post-CC snapshot, two different approaches have been adopted to determine the best-fit King solution: (1) the entire observed profile has been considered (central panel, cyan circles), (2) only the data points beyond 5″ from the center have been included in the fit (right panel, cyan circles), while the innermost portion of the profile (yellow circles) has been described through a linear fit (black dashed line). The positions of the core, half-mass, and tidal radii are marked, respectively, by dashed, dotted–dashed, and dotted vertical lines, and their values are labeled in the legend together with that of the concentration parameter.

3. Results

3.1. Projected Density Profile

As a first step in our analysis, we studied the projected density profile of the simulated cluster at different epochs, to verify whether a central cusp develops at t_{CC}, as expected, and how it evolves with time. To this purpose, we followed the same procedure adopted in several observational works determining the radial distribution of stellar number counts per unit area, $\Sigma_*(R)$, instead of the surface brightness profile (e.g., Miocchi et al. 2013; Lanzoni et al. 2019). Summarizing: (i) only stars brighter than one magnitude below the MSTO (i.e., with $V < V_{TO} + 1$) have been taken into account; (ii) the sampled area has been divided into concentric annuli centered on the cluster center, assumed to be at coordinates (0, 0), and (iii) each annulus has been typically partitioned into four subsectors. The exact number of annuli and subsectors is chosen as a compromise between including a sufficiently large number of stars to provide enough statistics, and a good radial sampling of the profile. Thus, it was set according to the (time-evolving) structure of the system. The projected cluster density at every radial distance from the center was then determined as the average number density of particles in the adopted subsectors, and its uncertainty was estimated from the variance among the subsectors. For the sake of illustration, in Figure 2 we show the projected star density profile obtained for two representative snapshots: one determined at $t = 7$ Gyr, during the pre-CC evolution (left panel), the second obtained for $t = 13.8$ Gyr, slightly after CC (middle and right panels). As expected, the central portion of the former is flat, while a significant density cusp, following a steep power-law behavior, is clearly visible toward the cluster center in the post-CC case.

Following what is commonly done in observational works (e.g., Miocchi et al. 2013; Lanzoni et al. 2019), we then searched for the single-mass King (1966) model that best fits the density profile obtained in the various snapshots. We explored a grid of models with dimensionless parameter W_0 (which is proportional to the gravitational potential at the center of the system) varying between 4 and 10.75 in steps of 0.05, corresponding to a concentration parameter c spanning the interval between 0.84 and 2.5. This parameter is defined as $c = \log(r_t/r_0)$, where r_t is the truncation or tidal radius of the system and r_0 is the characteristic scale length of the model named "King radius." The latter is often identified with the core radius R_c, which is the observationally accessible scale length corresponding to the distance from the center where the projected density is equal to half the central value. Indeed, they are quite similar, especially for large values of W_0 or c: the ratio R_c/r_0 varies between ∼0.82 for $c = 0.84$ and ∼0.99 for $c = 2.5$. We adopted the χ^2 approach described in detail in Lanzoni et al. (2019, see also Miocchi et al. 2013) to determine the best-fit solution (i.e., the one minimizing the residuals between the model and the "observed" profile) and to estimate the uncertainties of the best-fit parameters.

In agreement with what is found observationally for most GCs, we conclude that the King model family well reproduces the projected density profiles of pre-CC systems, while it shows a clear inconsistency in the innermost region of CC and post-CC snapshots. Figure 2 illustrates the result for the pre-CC case and the post-CC case discussed above. The best-fit King model is shown as a thick red line, while its uncertainty is represented by the shaded area and corresponds to the set of King models built by varying the fitting parameters within their uncertainty ranges. The King model function excellently reproduces the observed profile at any distance from the cluster center for the

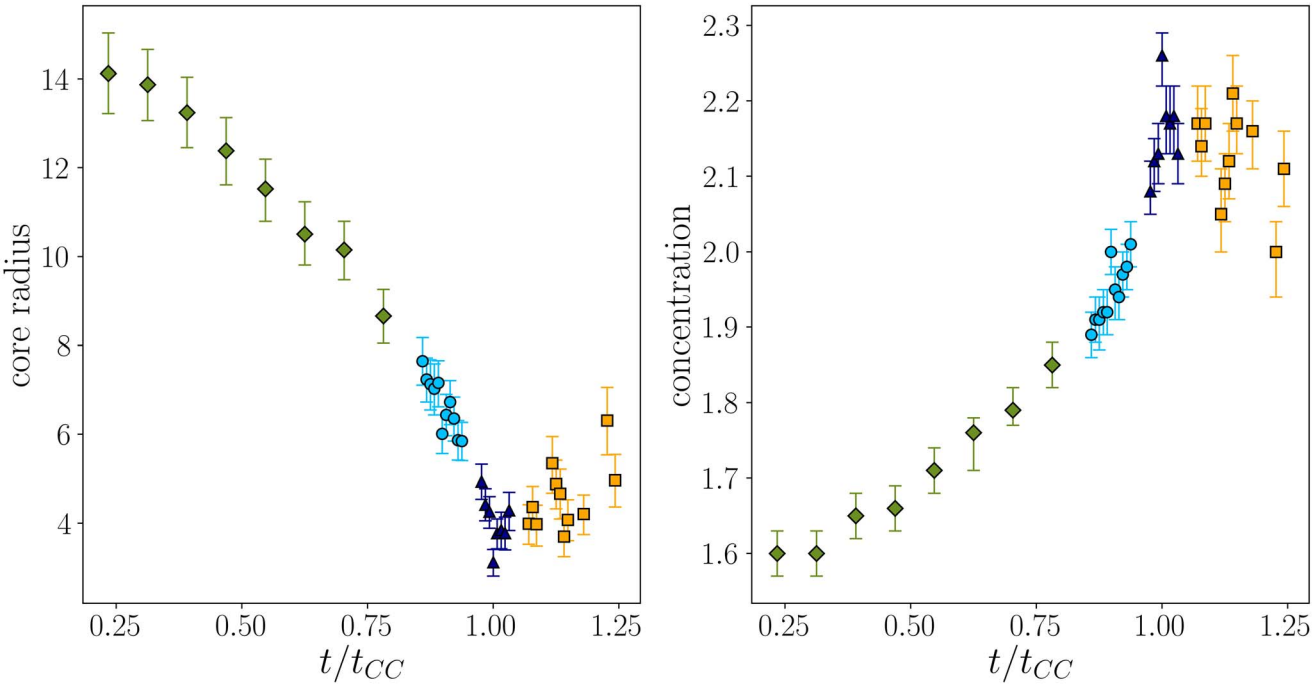

Figure 3. Time evolution of the core radius (left panel) and concentration parameter (right panel) as obtained from the King model fit to the entire star density profile of all the extracted snapshots. Different colors and symbols mark different evolutionary stages: green diamonds, cyan circles, blue triangles, and yellow squares for early, pre-CC, CC, and post-CC, respectively (the color code is the same as in Figure 1).

pre-CC snapshot (left panel). Conversely, being constant at small radii by construction, it cannot properly describe the central density cusp observed at $t = 13.8$ Gyr, after CC (central panel). Hence, in the presence of a central density cusp two different approaches are possible: either (1) to fit the entire density profile and search for the model providing the best solution regardless of its inadequacy in the region close to the center, or (2) to exclude from the fit the innermost portion of the density profile (here we assumed $R < 5''$ as a reasonable value). The central panel of Figure 2 corresponds to approach (1), while the right-hand panel shows the result of approach (2). The latter, combined with a linear fit to the innermost data points (oblique dashed line in the figure), clearly allows a much better description of the complex shape of the star density profile of CC and post-CC systems, but it depends on the (arbitrary) choice of the size of the region to be excluded from the King fit and it provides parameters (such as R_c, r_h, and c) that are not representative of the real cluster structure. Approach (1) clearly provides a poor representation of the central density profile, but it offers the advantage of being free from arbitrariness, thus allowing a coherent analysis of the density profile irrespective of the cluster dynamical stage.

Although defining a core region (with constant density) is formally meaningless for CC and post-CC systems, the time behavior of R_c and c obtained from approach (1) is qualitatively consistent with that of the 1% Lagrangian radius. This is illustrated in Figure 3, showing that the core radius progressively decreases to a minimum value at t_{CC}, then stays almost constant with increasing time, similarly to the trend of $r_{1\%}$ shown in Figure 1. The concentration parameter c displays the opposite behavior, and when the power-law cusp develops, during and after CC, it reaches values larger than $\sim$2. The time evolution of these parameters is in agreement with previous findings (e.g., Heggie et al. 2006; Trenti et al. 2010). Indeed a concentration parameter $c \sim 2$–2.5 and the presence of a central cusp in the density profile are the two diagnostics commonly used in the literature to classify a GC as CC or post-CC (see, e.g., Djorgovski & King 1984; Lugger et al. 1995; Ferraro et al. 2009).

To properly explore the development and transformation of the central cusp in the simulations, we show in Figure 4 the star density profile of the latest 16 snapshots, sampling the last 6 Gyr of evolution (from 10 to 16 Gyr). To facilitate the comparison, all the profiles have been vertically shifted until their density at $R = 65''$ matches the one measured in the $t = 10$ Gyr snapshot, with $65''$ ($\sim$3 pc) roughly corresponding to the value of the tridimensional half-mass radius of the 10 Gyr best-fit King model, which is represented in all panels as a black solid line. The color code is the same as adopted in Figure 1 to flag the dynamical stage of the selected snapshots. The first two panels show that $\sim$3 and 2 Gyr before CC, respectively, the star density profile is well reproduced by the King model. The third panel samples the CC event and the setting of the cusp. The remaining 13 panels probe the gravothermal oscillation phase. As can be seen, once set, the central cusp remains visible in the whole post-CC evolution (yellow profiles). This is the first relevant result of the present analysis, since it clearly demonstrates that the central cusp, once set, never disappears, in spite of the subsequent core radius oscillations. Hence, we can conclude that the density profile of star clusters is characterized by the presence of a central cusp also during the post-CC gravothermal oscillation phase.

However, the simulation also shows that the cusp's slope varies in time during the post-CC stage and the cusp becomes shallower during the expansion phases of gravothermal oscillations, thus raising the problem of its operational detectability and proper characterization. Indeed, the detection of the cusp and its correct measurement are among the most critical issues from the observational point of view. The

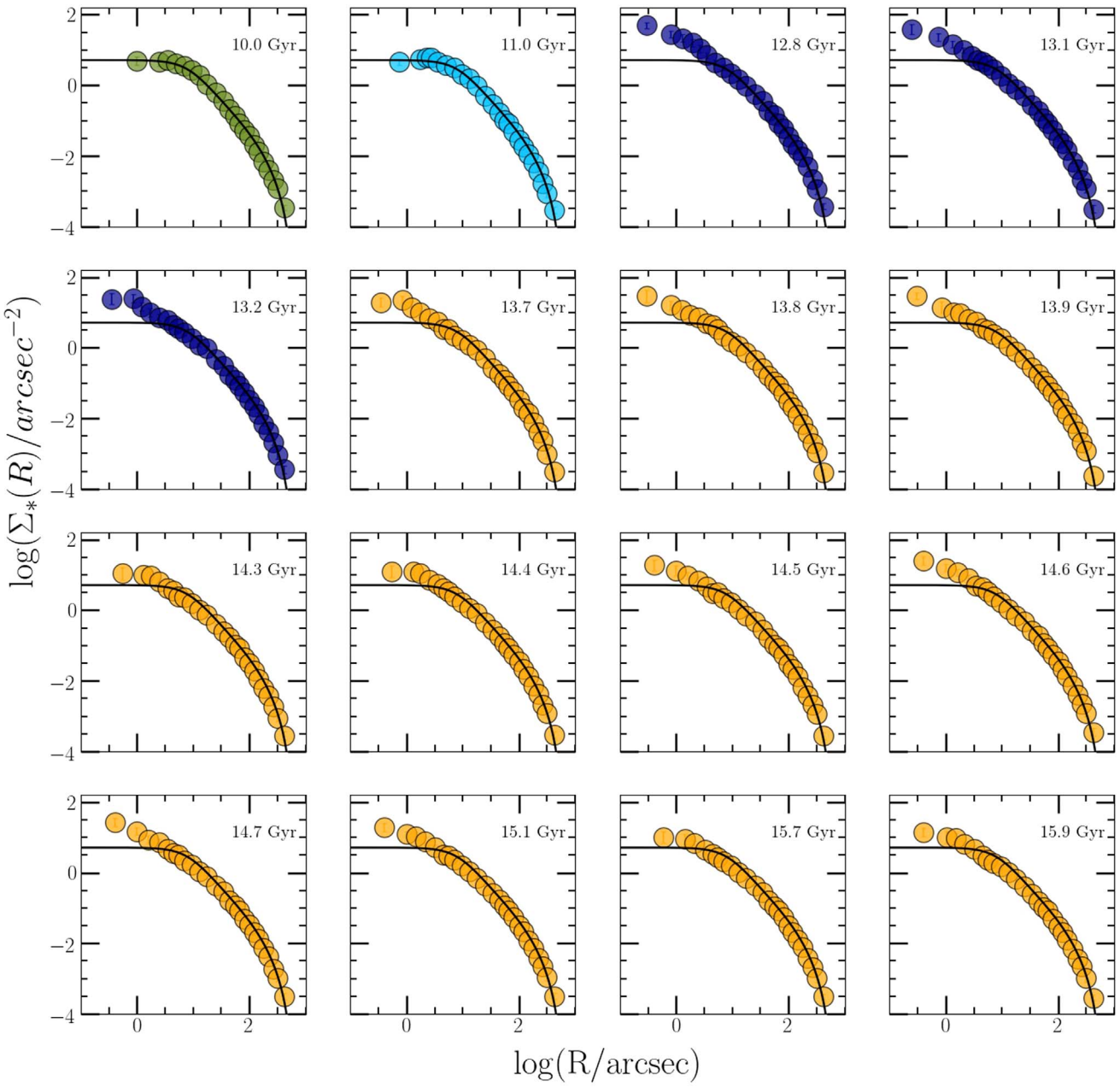

Figure 4. Comparison among the projected star density profiles measured during the latest stages of dynamical evolution, illustrating the appearance and persistence of the central cusp. All the profiles are normalized to the density measured at $R = 65''$ in the 10 Gyr snapshot, and the black solid line is the best-fit King model to the 10 Gyr density profile. The color code is as in Figure 1: cyan for pre-CC snapshots, blue for the CC phase, and yellow for post-CC stages; the snapshot time is labeled in each panel.

photometric incompleteness of the catalog, which becomes increasingly severe in the innermost cluster regions, artificially decreases the number of resolved stars close to the center. Thus, an appropriate assessment of the level of completeness of the observational sample is a key step to firmly establish the existence and the entity of the cusp. If the density profile is built with methods similar to that described above, but the observations used are too shallow, the resulting low statistics may force the use of radial bins that are too large, which directly affects the ability to detect the cusp. Also the exact definition of the innermost cluster region where the cusp manifests itself can affect the significance of the deviation from a King (centrally flat) model. This region is not known a priori and different assumptions about its extent might lead to either an over- or underestimate of the cusp steepness. All this raises the need for new indicators of the internal dynamical state of dense stellar systems that do not depend on the detection of a central density cusp or the lack thereof.

3.2. The Normalized Cumulative Radial Distribution

Similar to the route followed to refine the definition of the "dynamical clock" based on BSSs (compare, e.g., Ferraro et al. 2012 with Lanzoni et al. 2016 and Ferraro et al. 2018), here we explore a new way to infer the dynamical evolutionary stage of a GC using the normalized cumulative radial distribution (nCRD) of its stellar population. In particular, for every simulation snapshot, we consider all the stars brighter than a

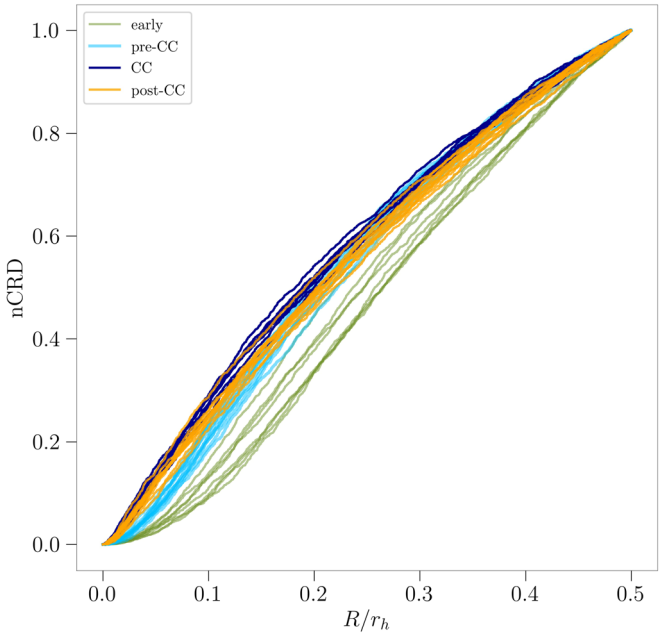

Figure 5. Normalized cumulative radial distributions of all the stars with $V \leq V_{\rm TO} + 0.5$ and $R < 0.5 \times r_h$ for all the analyzed simulation snapshots. The nCRDs are plotted according to the color code adopted in Figure 1: from early times (green), to pre-CC stages (cyan), the CC phase (blue), and the post-CC gravothermal oscillation epoch (yellow).

threshold $V_{\rm cut}$ located within a projected distance R_n from the center, and we determine their nCRD. By construction, this function varies between 0 (at $R = 0$) and 1 (at $R = R_n$), describing, for each value of R, the percentage of stars within that distance from the center (i.e., the number of stars counted within R normalized to the total number of stars within R_n). The magnitude cut has the purpose of mimicking the analysis of observed data sets, where it is needed to avoid photometric incompleteness biases and/or is set by the exposure time of the available images. Consistently with many observational studies, we adopted $V_{\rm cut} = V_{\rm TO} + 0.5$. The choice of a normalization radius (R_n) has the aim of referring the analysis to the same *physical* region in all snapshots, thus allowing a direct comparative evaluation of the effects of dynamical evolution in clusters of different sizes and at different dynamical stages. We built the nCRDs for several values of R_n, concluding that $R_n = 0.5 \times r_h$ is the best choice, because it maximizes the morphological differences that dynamical evolution imprints on the nCRD (see below), while still providing large statistics. Indeed, $0.5 \times r_h$ is a distance from the center small enough to be highly sensitive to dynamical evolutionary effects (which are strongest in the most central regions) and large enough to include large samples of stars. We emphasize that r_h is defined as the (tridimensional) radius of the sphere that includes half the total cluster mass, while $R_n = 0.5 \times r_h$ is the projected distance from the center within which stars are selected to build the nCRD. While r_h is not directly observable, its value is unambiguously obtained from the King model that, in projection, best fits the observed density profile. To avoid the arbitrariness of approach (2) to the fit of the star density profile (see discussion in Section 3.1), for all the snapshots we adopted the value of r_h obtained from the King model that best reproduces the entire density distribution (see an example in the central panel of Figure 2).

Figure 5 shows the nCRDs of all the considered snapshots, plotted with different colors according to the dynamical state, as in Figure 1. As can be seen, the nCRDs differ from each other and they do not appear to be randomly arranged: a nice progression of color groups following the aging sequence defined in Figure 1 is clearly visible, from green (early stages), to cyan, blue, and yellow (late, post-CC stages). This indicates that the nCRD of the cluster population is sensitive to the dynamical age of the parent cluster. As a consequence, the dynamical stage of a GC should be measurable from an appropriate parameterization of the morphology of its nCRD.

3.3. Defining the New Parameters

The result shown in Figure 5 clearly shows that the cluster dynamical aging is imprinted in the morphology of the nCRD of its stellar population. Both the percentage of stars within a given distance from the cluster center and the growth rate of the nCRD as a function of the clustercentric distance appear significantly different at different stages of dynamical evolution. Hence, both these quantities, in principle, could be used to quantify the dynamical state of a GC. Not surprisingly, the differences among the nCRDs appear more pronounced in the innermost radial portion of the system, where the effects of dynamical evolution are known to be stronger. We thus defined the following three parameters to quantify the nCRD differences:

(1) A_5—It is defined as the area subtended by each nCRD between the center ($R = 0$) and a projected distance equal to 5% of the tridimensional half-mass radius ($R = 0.05 \times r_h$), as illustrated by the shaded region in the left-hand panel of Figure 6. Because of the progressive increase in the central density during dynamical evolution, A_5 is expected to increase with time.

(2) P_5—It is defined as the value at $R = 0.05 \times r_h$ of the nCRD defined as above and it is illustrated in the central panel of Figure 6. The progressive contraction of the system toward CC translates into a centrally steeper nCRD and, as a consequence, the value of this parameter is also expected to increase as a function of the cluster dynamical age.

(3) $S_{2.5}$—It is defined as the slope of the straight line tangent to the nCRD at a projected distance equal to 2.5% of the half-mass radius ($R = 0.025 \times r_h$). Operationally, a polynomial function (in the form $y = ax^3 + bx^2 + cx$, with $x = R/r_h$) is fitted to the nCRD to smooth out its noisy behavior, and $S_{2.5}$ is the slope of the straight line tangent to the polynomial (see the red and the blue lines, respectively, in the right panel of Figure 6). Since our analysis showed that the most relevant changes in the growth rate of the nCRD occur in the very internal region of the system, $S_{2.5}$ has been defined at an even smaller projected distance from the center than the other two parameters (namely, at 2.5%, instead of 5%, the half-mass radius). It quantifies the radial growth rate of the nCRD, and similarly to A_5 and P_5 it is expected to increase as a function of the cluster dynamical age.

Following the definitions above, we measured the three parameters for all the snapshots under investigation. To estimate their uncertainties we took into account the dominant source of error, namely the uncertainty of the half-mass radius as obtained from the King fit to the density profile. To this end,

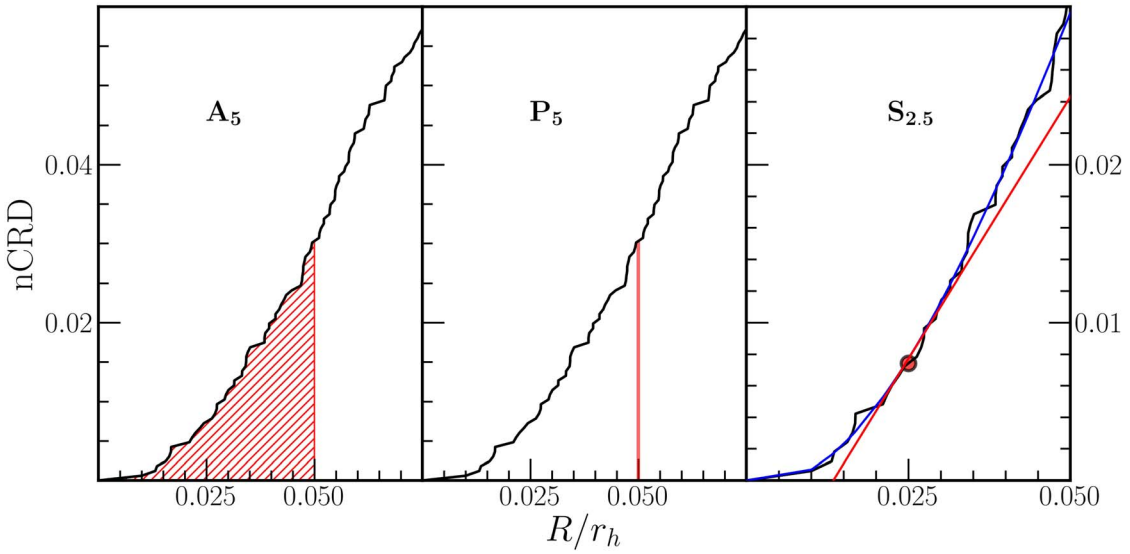

Figure 6. Definition of the three new diagnostics of dynamical evolution based on the nCRDs of the cluster stellar population shown in Figure 5. A_5 is the area subtended by the nCRD within a projected distance equal to 5% of the half-mass radius (red shaded region in the left panel). P_5 is the percentage of stars measured at $R = 0.05 \times r_h$, corresponding to the value of the nCRD at this clustercentric distance. $S_{2.5}$ is defined as the slope of the straight line tangent to the nCRD at $R = 2.5\%$ of the half-mass radius, as illustrated in the right panel: operationally, it is measured from the tangent line (red line) at $R = 0.025 \times r_h$ (large red circle) to the polynomial function that best reproduces the nCRD (blue line).

for every snapshot we redetermined the nCRD using all the stars with $V < V_{\rm cut}$ included within $R_n = 0.5 \times (r_h + \epsilon_h^+)$, where ϵ_h^+ is the upper error on r_h, and we measured the corresponding values of the three parameters. The difference between this value and that obtained for $R_n = 0.5 \times r_h$ is then adopted as the upper error on each parameter. To estimate the lower uncertainty we repeated the analogous procedure adopting $R_n = 0.5 \times (r_h - \epsilon_h^-)$, ϵ_h^- being the lower error on r_h. Figure 7 shows the time evolution of A_5 (top panel), P_5 (central panel), and $S_{2.5}$ (bottom panel). The time is normalized to $t_{\rm CC}$, which is also marked by the vertical red dashed line, and the snapshots are plotted according to the color code defined in Figure 1. As expected, all the parameters show an increasing trend with time. In addition, the trend is strikingly similar in the three cases: an almost constant behavior is observed at the early evolutionary times (green points), then a rapid increase occurs during the pre-CC stage (cyan points), up to the achievement of maximum values at the CC epoch (blue points), followed by the post-CC gravothermal oscillations stage, during which the parameters moderately fluctuate but remain stable slightly below the maximum reached at $t_{\rm CC}$ (yellow points). To elaborate, A_5 remains constant around $A_5 = 0.001$ for most of the time ($t \lesssim 0.8 t_{\rm CC}$), then it rapidly increases by a factor of 7 at CC, and it slightly decreases and fluctuates around $A_5 \sim 0.005$ later on. Similarly, the P_5 parameter stays essentially constant around $P_5 \sim 0.03$ in the early epochs, then the increasing stellar density in the cluster central regions increases it by a factor of 5 at CC, and finally the parameter stabilizes (with some fluctuations) around $P_5 \sim 0.12$ during the post-CC phase. An analogous evolutionary pattern is observed also for $S_{2.5}$: it is stable at $S_{2.5} \sim 0.3$ at early times, then it shows a rapid increase, by a factor of 6, reaching $S_{2.5} \sim 1.8$ at CC, and it further settles around $S_{2.5} \sim 1.3$, with the usual fluctuations, during the gravothermal oscillation stage.

3.4. Sensitivity of the Parameters to the Assumptions

Of course, the exact shape of the nCRD (and, consequently, the values of the newly defined parameters) depends on the assumptions used for its construction, in particular the values of radial distance (R_n) and the magnitude cut ($V_{\rm cut}$) adopted for selecting the star sample. In this section we thus explore the effects of modifying these values.

The (small) importance of varying R_n can already be noticed from the size of the errors associated with each parameter (see error bars in Figure 7). However, we also investigated the effect of a stronger variation, starting from the evidence that the King model best-fitting a pre-CC snapshot (in particular, the one extracted at 10 Gyr) well reproduces also the density profile observed at later times once the central cusp is excluded (see Figure 4). We thus assumed $R_n = 0.5 \times 65''$ for all snapshots, this value being half the cluster half-mass radius at 10 Gyr. The corresponding values of the three parameters are shown as triangles in Figure 8. The comparison with the values obtained by assuming the best-fit half-mass radius of each snapshot (circles, the same as in Figure 7) clearly confirms that the impact of R_n is negligible, at least for variations as large as $\sim$15% of its value.

As for the magnitude cut, the results shown so far have been obtained by adopting a relatively bright threshold, just half a magnitude below the MSTO: $V_{\rm cut} = V_{\rm TO} + 0.5$. This was done to allow the observational measurement of the nCRD parameters also in high-density GGCs, where reaching deeper limits with a reasonable level of completeness in the innermost regions of the system is still very hard, even with HST data. However, a fainter magnitude cut would include a significantly larger sample of stars, thus offering the advantage of larger statistics. We thus explored the nCRDs obtained with $V_{\rm cut} = V_{\rm TO} + 2$ and measured from them the three parameters defined above, to check whether they trace more or less efficiently the cluster dynamical aging. Figure 9 shows the comparison between the time evolution of A_5 as obtained for the two magnitude cuts: $V_{\rm cut} = V_{\rm TO} + 0.5$ in black and a limit

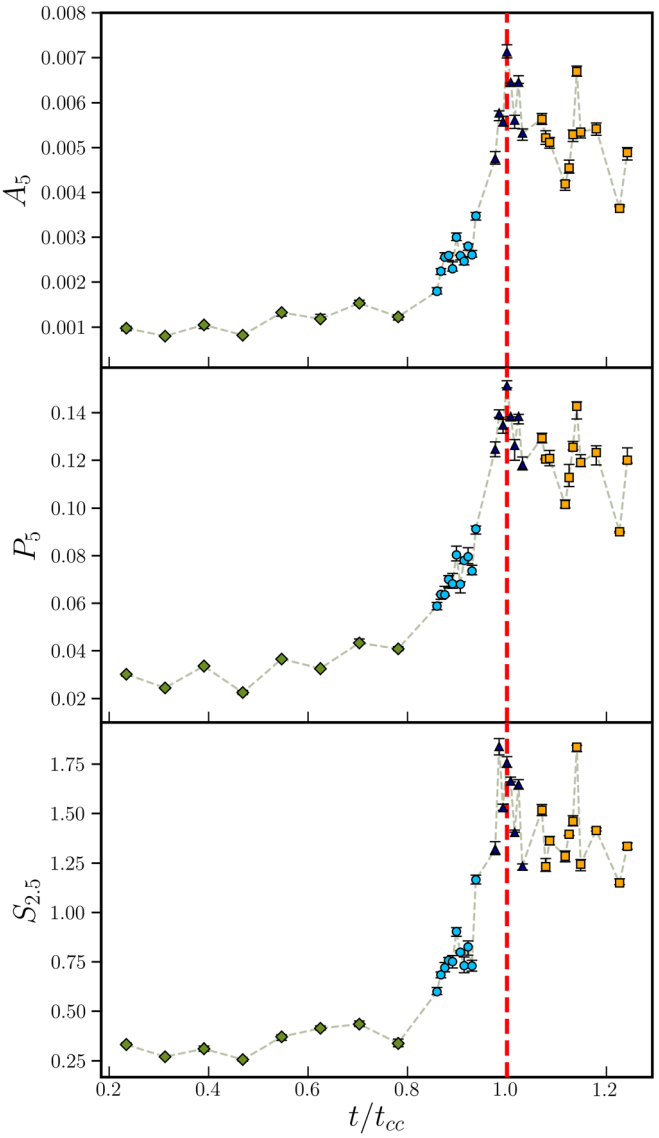

Figure 7. Time evolution of the nCRD parameters defined as in Figure 6 (see also Section 3.3): A_5 (top panel), P_5 (central panel) and $S_{2.5}$ (bottom panel). Time is normalized to t_{CC}, which is also marked by the vertical red dashed line. The symbol shapes and colors are as in Figure 3. All three parameters show an increasing trend with time, reaching their peak value at CC (blue triangles) and then remaining large and essentially constant, with some fluctuations, during the late, gravothermal oscillation stage (yellow squares).

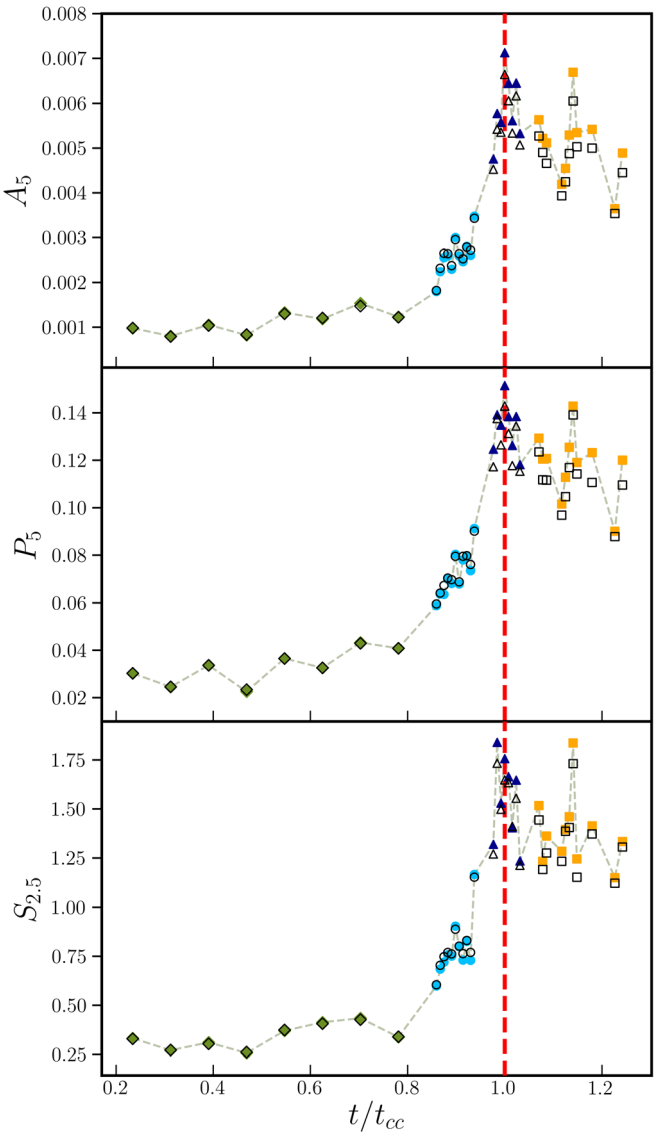

Figure 8. Comparison between the parameters obtained from nCRDs built using $R_n = 0.5 \times r_h$ (colored solid symbols, the same as in Figure 7) and those obtained from nCRDs built using $R_n = 0.5 \times 65''$ (empty symbols).

1.5 magnitudes fainter in red. As can be seen, the overall trend is perfectly consistent in the two cases, thus confirming that the increase in the A_5 parameter as a function of time does not depend on the details of its own definition, but traces instead the structural changes in the nCRD due to the effects of dynamical evolution. Indeed, the trend during the early and pre-CC phases is virtually indistinguishable in the two cases, except for a less noisy behavior for $V_{\rm cut} = V_{\rm TO} + 2$ due to the increased statistics. Instead, the sensitivity of A_5 during the CC and the post-CC phases appears systematically reduced in the case of the deeper magnitude cut, with an increase by a factor of $\sim$5 (instead of $\sim$7) with respect to the values measured in the early snapshots. This is consistent with the fact that assuming a fainter magnitude threshold corresponds to including stars of smaller masses in the analysis, which are less affected by the dynamical evolutionary processes occurring in the cluster center. Analogous dependences on the adopted magnitude cut are also found for the parameters P_5 and $S_{2.5}$. Hence, as a global result, we conclude that the sensitivity of the nCRD parameters to the cluster dynamical evolution tends to decrease with fainter magnitude cuts, and $V_{\rm cut} = V_{\rm TO} + 0.5$, in spite of smaller numbers of stars, looks to be the best compromise between large enough statistics and good efficiency to distinguish among different dynamical evolutionary stages.

4. Discussion and Summary

In this paper we have presented the first results of a study aimed at defining new empirical parameters that use the inner radial distribution of cluster stars to characterize the different dynamical evolutionary phases experienced by dense stellar systems. To this end, we have used a Monte Carlo simulation following the "typical" dynamical evolution of a GC, from an initial progressive contraction of the core, to the CC event, and the gravothermal oscillations during the post-CC phase.

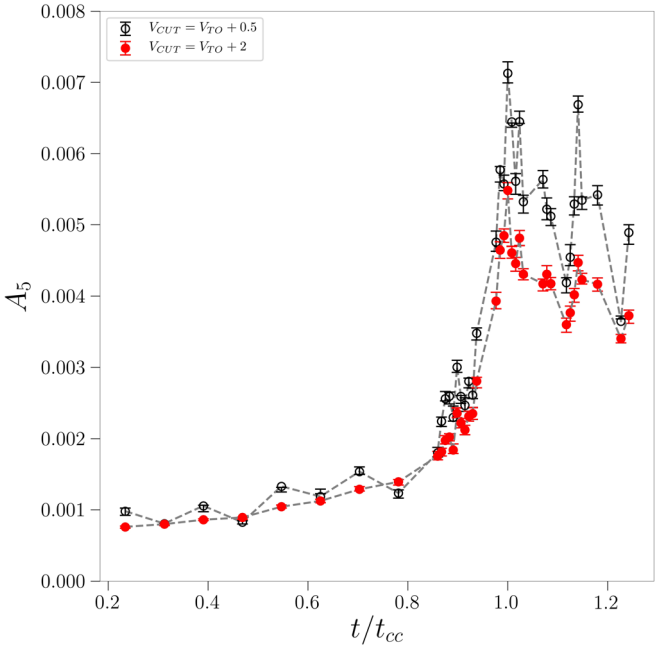

Figure 9. Time evolution of the A_5 parameter measured from the nCRDs built with different magnitude cuts: $V_{\rm cut} = V_{\rm TO} + 0.5$ (empty black circles) and $V_{\rm cut} = V_{\rm TO} + 2$ (solid red circles).

A total of 38 time snapshots sampling these different stages have been extracted from the simulation and analyzed by closely following the steps usually taken in the analysis of an observational data set. We used only projected (instead of three-dimensional) quantities and a reasonable cut in magnitude to mimic the observational approach, where photometric incompleteness and/or exposure times can severely limit the extent in magnitude of the sample. In addition, the same approach used in observational works has been applied to the numerical data for determining the star density profile and its best-fit King solution. The analysis of the star density profiles extracted from the simulation shows that the central cusp developing during CC is not erased by the subsequent gravothermal oscillations; hence the central cusp remains as a stable feature and characterizes the star density profile also during the post-CC phase. However, a preliminary inspection of the simulations shows that the slope of the central cup can vary during the post-CC phase and its operational detectability from observed data may present some difficulties. A study aimed at a detailed characterization of the key properties of the central density cusp will be the specific subject of a future paper (B. Bhat et al., 2021, in preparation).

We then used the simulation to explore new ways of determining the dynamical evolutionary stage of star clusters from the global properties of their stellar population (instead of specific exotic species such as, e.g., BSSs). To this purpose we constructed and analyzed the nCRD of each snapshot using all the stars brighter than 0.5 magnitudes below the MSTO and located within a projected distance $R_n = 0.5 \times r_h$ from the center (see Section 3.2). These showed an intriguing level of sensitivity to the dynamical evolution of the cluster. Indeed, the shape of the nCRDs varies significantly as a function of the cluster dynamical state and allows a clear identification of the various fundamental stages of the evolution of a cluster (the pre-CC, the CC, and the post-CC phases). We have introduced three parameters (named A_5, P_5, and $S_{2.5}$) that quantify the morphological changes in the nCRD as a function of time and turned out to be effective diagnostics of the cluster dynamical age. The three parameters show similar trends with time, mirroring the dynamical evolution of the host cluster. After an early phase (lasting $\sim$8 Gyr in our simulation) in which they are essentially constant, they rapidly increase, reaching a maximum at the CC epoch. We estimate that, as the cluster approaches CC, they grow by a factor of 5–7. The post-CC evolution exhibits a slight decrease in the values of all the parameters. However, in spite of some fluctuations, their average value remains significantly larger than those typical of the pre-CC phase. From an observational point of view this is one of the most relevant aspects. Indeed, the fact that the values of the parameters in the post-CC stages remain significantly larger than those in the early phases offers the concrete possibility of clearly distinguishing highly evolved GCs also in those cases where the detection of the central density cusp is uncertain.

The results of this first exploratory work pave the way to a series of future investigations in which we will broaden the range of initial conditions and study their impact on the empirical parameters defined here. By changing the initial structural properties of the simulated clusters, we will compare the three parameters determined in stellar systems that, after one Hubble time of evolution, have reached different dynamical states. We will also include populations of primordial binaries, which are known to halt the core contraction earlier in the cluster evolution and at lower concentrations (see, e.g., Vesperini & Chernoff 1994; Trenti et al. 2007; Chatterjee et al. 2010). The main differences between the values of A_5, P_5, and $S_{2.5}$ in simulations with and without primordial binaries are expected during the advanced phases of the evolution, toward CC and post-CC, when the milder contraction of the clusters with primordial binaries might lead to a different and/or less extreme evolution of these parameters. The study presented here will also be further extended to explore the effects of different retention fractions of dark remnants (neutron stars and black holes; see, e.g., Alessandrini et al. 2016; Giersz et al. 2019; Kremer et al. 2020, 2021; Gieles et al. 2021, for some studies on the dynamical effects of dark remnants). Finally, a forthcoming paper will be dedicated to building nCRDs and determining the three parameters here defined in a sample of observed star clusters. This requires photometric observations (i) with a high enough angular resolution to resolve individual stars even in the innermost cluster regions, (ii) sampling each system at least out to $0.5 \times r_h$, and (iii) deep enough to reach a few magnitudes below the MSTO. These requirements are achieved by most HST and adaptive-optics-assisted observations currently available for many GCs, thus making the determination of the three parameters from observations relatively straightforward, although particular care is needed to deal with typical observational difficulties such as photometric incompleteness, differential reddening, and Galactic field contamination. We will discuss the relation between these parameters and other dynamical indicators (in particular, the A^+ parameter measured from BSSs; see the Introduction), thus providing quantitative assessments of the operational ability of the three nCRD diagnostics to distinguish dynamically young GCs from systems in advanced states of dynamical evolution.

We thank the anonymous referee for comments and suggestions that helped us to improve the paper. This work is

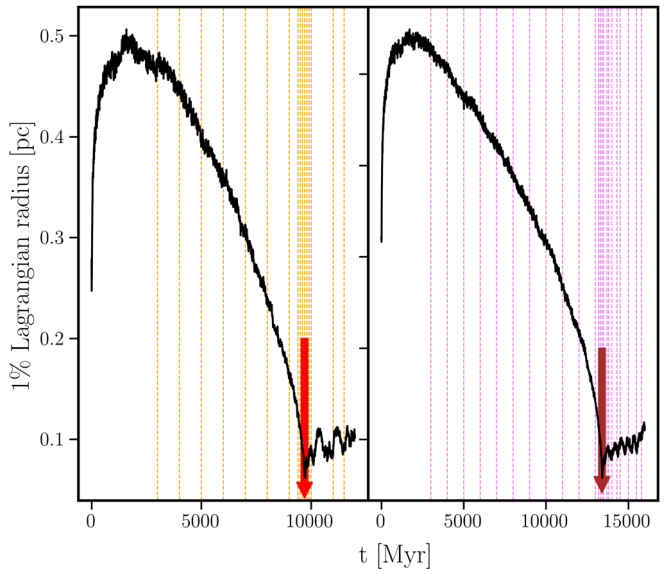

Figure 10. Time evolution of the 1% Lagrangian radius (in parsecs) in the 250k simulation (yellow, left panel) and the W05 run (magenta, right panel). The vertical lines correspond to the time snapshots for which we determined the values of A_5, P_5, and $S_{2.5}$ shown in Figure 11. The CC time is marked with a large red arrow: $t_{CC} = 9.7$ Gyr in the 250k run (left panel), $t_{CC} = 13.4$ Gyr in the W05 simulation (right panel).

part of the project Cosmic-Lab at the Physics and Astronomy Department "A. Righi" of the Bologna University (http://www.cosmic-lab.eu/Cosmic-Lab/Home.html). The research was funded by the MIUR throughout the PRIN-2017 grant awarded to the project Light-on-Dark (PI: Ferraro) through contract PRIN-2017K7REXT.

Appendix
Simulations with Different Initial Conditions

The parameter space of possible initial conditions for realistic simulations of GCs is huge, including variations in the initial values of W_0, scale radii, number of stars, primordial binary fraction, and dark remnant retention fraction. Hence, a series of forthcoming papers will be devoted to accurately exploring the effects that different initial conditions can have on the values of the three proposed new indicators and their time evolution.

In this appendix we present just a first investigation of this issue, by analyzing two additional simulations where only one initial condition is varied at a time, with respect to the reference run discussed in the main text (hereafter, REF run). In the first one (hereafter, W05 run), we changed the value of the King dimensionless potential ($W_0 = 5$), while keeping the same initial number of stars and half-mass radius, and assuming the same Galactocentric distance as in the reference simulation. In the second run (hereafter, 250k run), we have followed the evolution of a system with half of the number of particles ($N = 250{,}000$) and kept the same W_0, half-mass radius, and Galactocentric distance used for the REF simulation. The initial mass in the W05 run is the same as in the REF model, while it is $\sim 1.6 \times 10^5$ $M_\odot$ initially in the 250k simulation (and $\sim 5.7 \times 10^4$ $M_\odot$ at 12 Gyr). Figure 10 shows the time evolution of the 1% Lagrangian radius of these two simulations. The overall trend is very similar to that shown in Figure 1 for the REF run. However, CC occurs earlier (at $t_{CC} = 9.7$ Gyr) in the case of the less massive cluster (250k run; left panel), while it is delayed by almost 1 Gyr for the initially less concentrated cluster (W05 run, where $t_{CC} = 13.4$ Gyr; right panel). The vertical lines mark the time snapshots extracted from these simulations, which have been analyzed following the same procedures and adopting the same assumptions as discussed in the main text for the REF simulation.

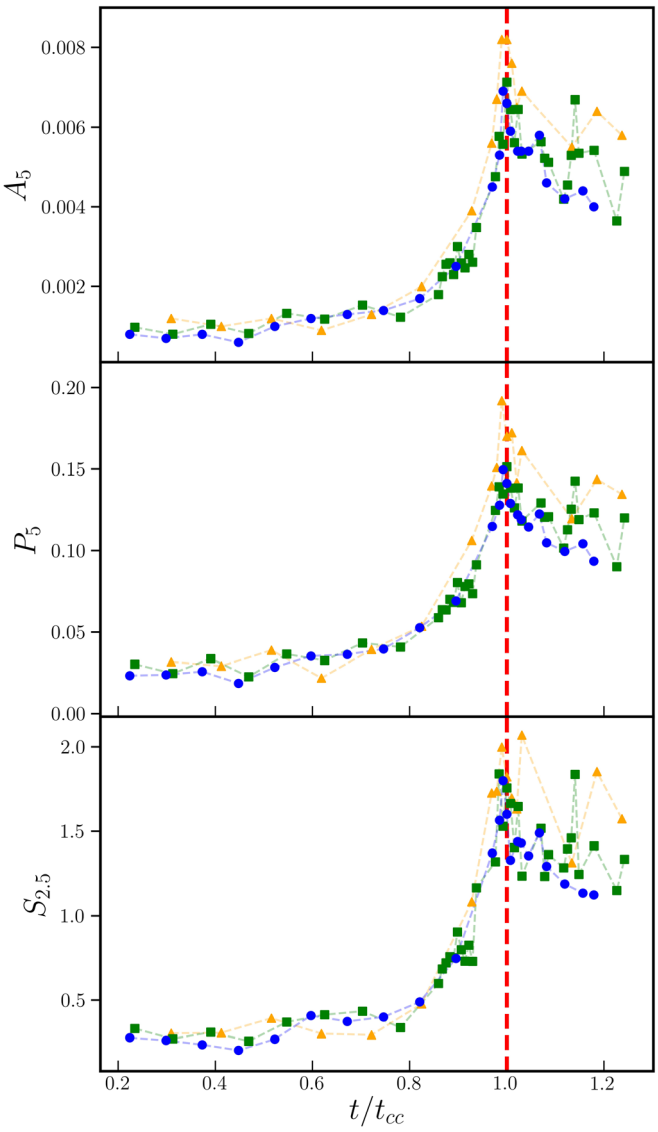

Figure 11. Time evolution of the nCRD parameters in simulations 250k (yellow triangles), W05 (blue circles), and REF (green squares, the same points as in Figure 7). From top to bottom, the three panels refer to parameters A_5, P_5, and $S_{2.5}$. Time is normalized to each respective value of t_{CC}.

The resulting time dependence of the three parameters is shown in Figure 11, where the yellow circles correspond to the 250k simulation, the blue circles refer to the W05 run, and, for the sake of comparison, we overplotted also the results of the REF simulation in green (same points as in Figure 7). Along the x-axis, the time is normalized to the respective values of t_{CC}. The comparison shows that the differences among the adopted initial conditions have a negligible effect on both the absolute values and the time dependence of the three parameters, thus further reinforcing the conclusion that A_5, P_5, and $S_{2.5}$ are powerful indicators of GC internal dynamical evolution.

ORCID iDs

B. Bhat https://orcid.org/0000-0002-3578-6037
B. Lanzoni https://orcid.org/0000-0001-5613-4938
F. R. Ferraro https://orcid.org/0000-0002-2165-8528
E. Vesperini https://orcid.org/0000-0003-2742-6872

References

Alessandrini, E., Lanzoni, B., Ferraro, F. R., Miocchi, P., & Vesperini, E. 2016, ApJ, 833, 252
Baumgardt, H., & Makino, J. 2003, MNRAS, 340, 227
Baumgardt, H., & Vasiliev, E. 2021, MNRAS, 505, 5957
Beccari, G., Ferraro, F. R., Dalessandro, E., et al. 2019, ApJ, 876, 87
Bianchini, P., van de Ven, G., Norris, M. A., Schinnerer, E., & Varri, A. L. 2016, MNRAS, 458, 3644
Bianchini, P., Webb, J. J., Sills, A., & Vesperini, E. 2018, MNRAS, 475, L96
Chatterjee, S., Fregeau, J. M., Umbreit, S., & Rasio, F. A. 2010, ApJ, 719, 915
Cohen, R. E., Bellini, A., Libralato, M., et al. 2021, AJ, 161, 41
Dalessandro, E., Ferraro, F. R., Massari, D., et al. 2013, ApJ, 778, 135
Djorgovski, S. 1993, in ASP Conf. Ser., 50, Structure and Dynamics of Globular Clusters, ed. S. G. Djorgovski & G. Meylan (San Francisco, CA: ASP), 373
Djorgovski, S., & King, I. R. 1984, ApJL, 277, L49
Ferraro, F. R., Beccari, G., Dalessandro, E., et al. 2009, Natur, 462, 1028
Ferraro, F. R., Lanzoni, B., Dalessandro, E., et al. 2012, Natur, 492, 393
Ferraro, F. R., Lanzoni, B., Dalessandro, E., et al. 2019, NatAs, 3, 1149
Ferraro, F. R., Lanzoni, B., & Dalessandro, E. 2020, RLSFN, 31, 19
Ferraro, F. R., Lanzoni, B., Raso, S., et al. 2018, ApJ, 860, 36
Ferraro, F. R., Paltrinieri, B., Fusi Pecci, F., et al. 1997, A&A, 324, 915
Ferraro, F. R., Possenti, A., Sabbi, E., et al. 2003, ApJ, 595, 179
Ferraro, F. R., Sabbi, E., Gratton, R., et al. 2006, ApJL, 647, L53
Fiorentino, G., Lanzoni, B., Dalessandro, E., et al. 2014, ApJ, 783, 34
Forbes, D. A., & Bridges, T. 2010, MNRAS, 404, 1203
Gieles, M., Erkal, D., Antonini, F., Balbinot, E., & Peñarrubia, J. 2021, NatAs, 5, 957
Giersz, M., Askar, A., Wang, L., et al. 2019, MNRAS, 487, 2412
Giersz, M., Heggie, D. C., Hurley, J. R., & Hypki, A. 2013, MNRAS, 431, 2184
Harris, W. E. 1996, AJ, 112, 1487
Heggie, D. C., Trenti, M., & Hut, P. 2006, MNRAS, 368, 677
Hills, J. G., & Day, C. A. 1976, ApJL, 17, 87
Hobbs, G., Lorimer, D. R., Lyne, A. G., & Kramer, M. 2005, MNRAS, 360, 974
Hurley, J. R., Pols, O. R., & Tout, C. A. 2000, MNRAS, 315, 543
Hurley, J. R., Tout, C. A., & Pols, O. R. 2002, MNRAS, 329, 897
Hypki, A., & Giersz, M. 2013, MNRAS, 429, 1221
King, I. R. 1966, AJ, 71, 64
Kremer, K., Rui, N. Z., Weatherford, N. C., et al. 2021, ApJ, 917, 28
Kremer, K., Ye, C. S., Rui, N. Z., et al. 2020, ApJS, 247, 48
Kroupa, P. 2001, MNRAS, 322, 231
Lanzoni, B., Dalessandro, E., Ferraro, F. R., et al. 2007a, ApJL, 668, L139
Lanzoni, B., Ferraro, F. R., Alessandrini, E., et al. 2016, ApJL, 833, L29
Lanzoni, B., Ferraro, F. R., Dalessandro, E., et al. 2010, ApJ, 717, 653
Lanzoni, B., Ferraro, F. R., Dalessandro, E., et al. 2019, ApJ, 887, 176
Lanzoni, B., Sanna, N., Ferraro, F. R., et al. 2007b, ApJ, 663, 1040
Leonard, P. J. T. 1996, ApJ, 470, 521
Libralato, M., Bellini, A., Piotto, G., et al. 2019, ApJ, 873, 109
Libralato, M., Bellini, A., van der Marel, R. P., et al. 2018, ApJ, 861, 99
Lombardi, J. C. J., Rasio, F. A., & Shapiro, S. L. 1995, ApJL, 445, L117
Lugger, P. M., Cohn, H. N., & Grindlay, J. E. 1995, ApJ, 439, 191
Marín-Franch, A., Aparicio, A., Piotto, G., et al. 2009, ApJ, 694, 1498
McCrea, W. H. 1964, MNRAS, 128, 147
Meylan, G., & Heggie, D. C. 1997, A&ARv, 8, 1
Miocchi, P., Lanzoni, B., Ferraro, F. R., et al. 2013, ApJ, 774, 151
Pooley, D., Lewin, W. H. G., Anderson, S. F., et al. 2003, ApJL, 591, L131
Portegies Zwart, S. 2019, A&A, 621, L10
Ransom, S. M., Hessels, J. W. T., Stairs, I. H., et al. 2005, Sci, 307, 892
Raso, S., Pallanca, C., Ferraro, F. R., et al. 2019, ApJ, 879, 56
Sills, A., Adams, T., & Davies, M. B. 2005, MNRAS, 358, 716
Spitzer, L. 1987, Dynamical Evolution of Globular Clusters (Princeton, NJ: Princeton Univ. Press)
Tiongco, M. A., Vesperini, E., & Varri, A. L. 2016, MNRAS, 461, 402
Trenti, M., Heggie, D. C., & Hut, P. 2007, MNRAS, 374, 344
Trenti, M., Vesperini, E., & Pasquato, M. 2010, ApJ, 708, 1598
Vesperini, E., & Chernoff, D. F. 1994, ApJ, 431, 231
Webb, J. J., & Vesperini, E. 2017, MNRAS, 464, 1977